EDGE ARTICLE

Check for updates

H₂O₂ accumulation promoting internalization of ox-LDL in early atherosclerosis revealed *via* a synergistic dual-functional NIR fluorescence probe†

Hui Wang,‡*[a] Jingjing Guo,‡[a] Tiancong Xiu,[a] Yue Tang,*[d] Ping Li, [ID] *[ac] Wei Zhang,[a] Wen Zhang [ID] [a] and Bo Tang [ID] *[ab]

The equilibrium of lipid metabolism is critical to sustaining human health. Metabolic disorders often result in a variety of cardiovascular illnesses, especially atherosclerosis. Atherosclerosis is characterized by complicated complications and high mortality. Cholesterol deposition and oxidative stress have been considered as critical mechanisms in the occurrence and progression of atherosclerosis, however, the relationship between oxidative stress and lipid accumulation remains a puzzle in foam cells during the early stages of atherosclerosis development. Hydrogen peroxide (H₂O₂) has been reported to participate in various signaling pathways associated with atherosclerotic diseases. Additionally, the excessive intake of oxidized low-density lipoprotein (ox-LDL) leads to cholesterol accumulation and viscosity increasing in foam cells. Therefore, it is critical to investigate the internalization and modification of ox-LDL by H₂O₂ in foam cells. Herein, we developed a near-infrared, synergistic dual-functional fluorescent probe capable of detecting H₂O₂ and viscosity simultaneously with high selectivity and sensitivity. Through *in situ* imaging of H₂O₂ and viscosity *in vivo*, we discovered that H₂O₂ accumulation leads to an increased intake of ox-LDL in the early stages of plaque formation. This finding establishes a new experimental approach and theoretical foundation for the diagnosis and treatment of atherosclerosis, as well as the development of new medications.

Introduction

Lipids are one of the most important biomacromolecules in living systems, and they encompass a wide variety of molecules such as free fatty acids, fatty acid esters, sterols, phospholipids, and triglycerides.[1] When the equilibrium of their metabolism is disrupted by environmental or metabolic stress, lipids can become essential components of pathophysiological cascades that damage healthy cell and tissue function, which dysfunction will lead to various diseases, such as atherosclerosis, hyperlipemia, chronic inflammation and fatty liver.[2] When hyperlipidemia or inflammation-associated stimuli induce arterial endothelial cells to express adhesion molecules, leukocytes are recruited, along with the release of proinflammatory cytokines. Meanwhile, vascular endothelial permeability increases, and low-density lipoprotein (LDL) particles penetrate into the arterial wall and are oxidized to plenty of oxidized LDL (ox-LDL) by hydrogen peroxide (H₂O₂).[3] Macrophages ingest excess ox-LDL, leading to cholesterol accumulation, and eventually turn into foam cells.[4,5] Foam cells in the arterial wall are a hallmark of an early atherosclerotic lesion as they initiate plaque formation on blood arteries.[6] Atherosclerosis is defined by the deposition of cholesterol that forms the lipid core of plaques beneath the intima of the arterial wall, leading to arterial lumen narrowing and increased blood flow.[7] The incidence of atherosclerosis has recently risen worldwide, and the risk of serious complications including stroke caused by plaque rupture rises with age; therefore development of effective therapy of atherosclerosis could be beneficial to human health.[8,9]

To date, many commonly used anti-atherosclerosis drugs are still far from satisfactory. For example, aspirin, statins, and fibrate medications mainly contribute to reducing blood lipids,

[a]College of Chemistry, Chemical Engineering and Materials Science, Key Laboratory of Molecular and Nano Probes, Ministry of Education, Collaborative Innovation Center of Functionalized Probes for Chemical Imaging in Universities of Shandong, Institutes of Biomedical Sciences, Shandong Normal University, Jinan 250014, Shandong, China. E-mail: tangb@sdnu.edu.cn; lip@sdnu.edu.cn; hui_wang@sdnu.edu.cn

[b]People's Republic of China; Laoshan Laboratory, 168 Wenhai Middle Rd, Aoshanwei Jimo, Qingdao 266237, Shandong, China

[c]College of Chemistry and Chemical Engineering, Northwest Normal University, Lanzhou 730070, Gansu, China

[d]Department of Emergency Medicine, Shandong Provincial Clinical, Research Center for Emergency and Critical Care Medicine, Qilu Hospital of Shandong University, Jinan 250012, Shandong, China. E-mail: yuetang0531@hotmail.com

† Electronic supplementary information (ESI) available. See DOI: https://doi.org/10.1039/d4sc05546b

‡ These authors contributed equally.

stabilizing plaque, or inhibiting inflammation in artery blood vessels, but none of them can alleviate arterial lumen stenosis.[10] Since the appearance of foam cells is considered an early character during atherosclerotic plaque formation, exploring lipid-related signaling pathways in foam cells could be conducive to developing new anti-atherosclerotic drugs by providing potential targets.

Two important elements in the pathophysiology of atherosclerosis are cholesterol deposition and chronic inflammation.[11] It has been widely acknowledged that inflammation is intimately associated with oxidative stress.[12] Oxidative stress is considered a critical mechanism in the onset and progression of atherosclerosis. As the most stable reactive oxygen species (ROS), H_2O_2 is implicated to be involved in ox-LDL formation and indirectly modulates the expression of a large number of genes by regulating the NF-κB signaling pathway.[13,14] Previous studies had shown that the lowest concentration of H_2O_2 levels was close to 10 μM in the pathological environment of atherosclerosis.[15] In addition, along with cholesterol deposition in macrophages, the intracellular viscosity will be gradually elevated, and macrophages will transform into foam cells.[16,17] The increase in cellular H_2O_2 content and viscosity is a typical phenomenon in the early stage of foam cell formation. The accumulation of foam cells is a hallmark of early atherosclerotic plaque formation. However, the relationship between oxidative stress and lipid accumulation remains a puzzle in foam cells. Therefore, it is critical to investigate the internalization and modification of ox-LDL by H_2O_2 in foam cells in the early stages of atherosclerosis development, but little research has been conducted in this area.

Based on the above, the development of novel methods for simultaneous detection of H_2O_2 levels with viscosity changes could not only indicate foam cell formation, but also may resolve the signaling pathways associated with oxidative stress-caused lipid accumulation during foam cell formation. In the past decade, fluorescent imaging has been widely applied for the detection of bioactive molecules due to its advantages of high sensitivity, good selectivity and allowing real-time imaging *in situ*.[18–21] Many fluorescent probes for the single/double detection of ROS or viscosity have been reported by Lin's group,[22] Ma's group[23] and Tang's group,[24–26] and they successfully used these probes *in vivo* (Table S1†). In addition, many studies on fluorescence imaging of atherosclerosis have also been reported in recent years,[27–36] but small-molecule fluorescent probes with dependent excitation and emission wavelengths for real-time and simultaneous imaging of H_2O_2 and viscosity in atherosclerotic plaques have not been developed so far.

Herein, a novel near-infrared dual-functional fluorescence probe, **HV-AS**, was designed for synergistic fluorescent imaging of H_2O_2 and viscosity using independent emission wavelengths. In our strategy, an α,β-unsaturated malonitrile moiety was conjugated to the hemicyanine framework through a C–C bond, and a *p*-phenyl boronic acid ester moiety was selected as the H_2O_2 reactive site, coupled to hemicyanine by ether connection. The α,β-unsaturated malonitrile moiety disrupts the coplanarity of the whole molecule.[37–40] In a low viscosity environment, the rotor freely revolves around the large conjugate structure of hemicyanine, dissipating the excited state energy of the **HV-AS** through non-radiation and quenching its fluorescence. Viscosity rises cause the rotor's free rotation to be restricted. This leads to the expansion of **HV-AS** coplanarity, which results in a redshifted emission wavelength and enhanced fluorescence intensity. In the presence of H_2O_2, the boronic ester moiety reacts with H_2O_2 to expose a phenolic group, then a quinone derivative leaves, and a subsequent intramolecular cyclization reaction proceeds forming a coumarin derivative.[41,42] The enhanced conjugation effect caused a redshift of the fluorescence wavelength to the near-infrared region (from 660 nm to 680 nm after reaction with H_2O_2). Using **HV-AS**, we were able to observe the real-time changes of H_2O_2 and viscosity in foam cells and atherosclerotic plaques for the first time. By cell and *in vivo* fluorescence imaging experiments, the signaling pathways associated with oxidative stress-caused lipid accumulation during foam cell formation were ultimately resolved, and eventually, the source of H_2O_2 and H_2O_2 accumulation promoting ox-LDL internalization during foam cell formation were identified. This signaling was further demonstrated by feeding the mice setanaxib that reduced the generation of H_2O_2 and consequently prevented plaque development.
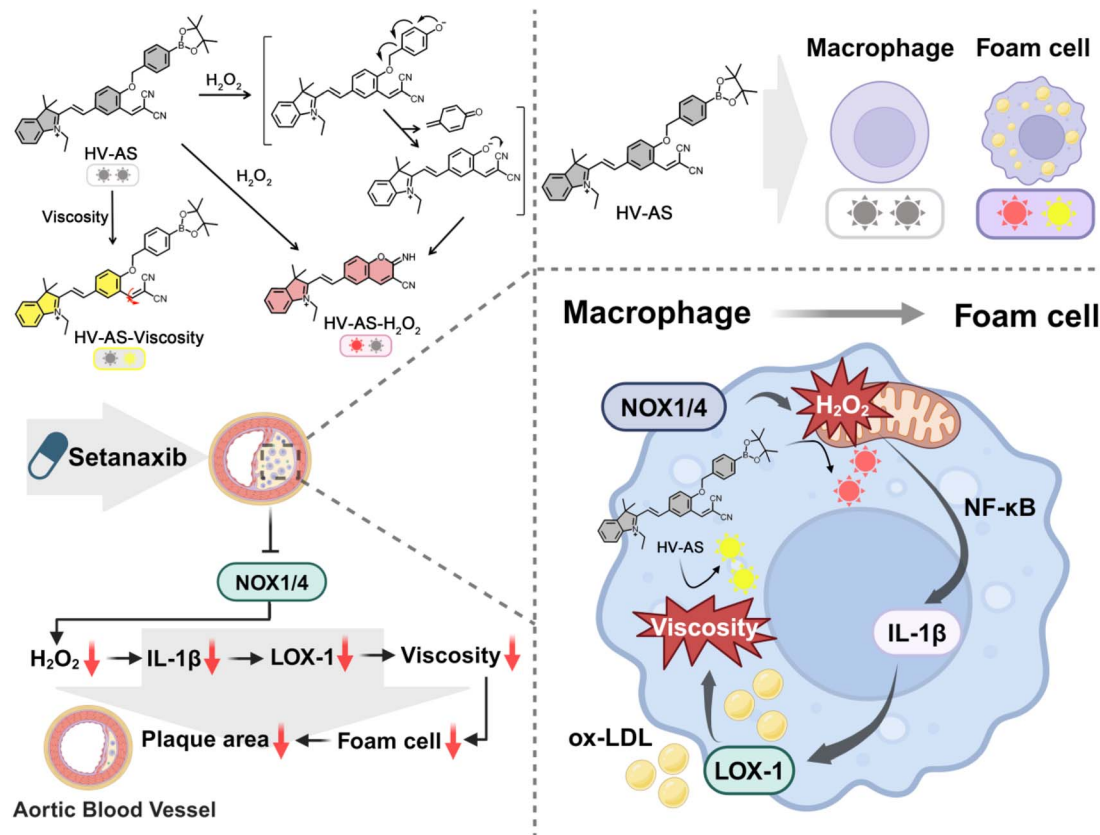
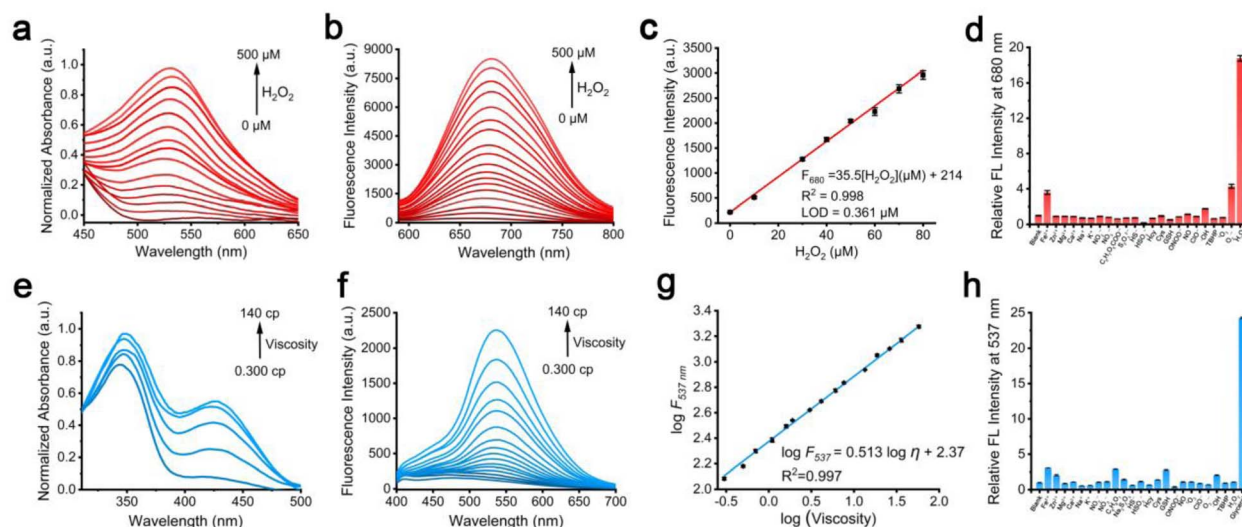## Results and discussion

Photophysical properties of HV-AS

The fluorescent probe **HV-AS** has been successfully synthesized. The synthetic route and responding mechanism are shown in Fig. S1–S3† and Scheme 1. The key intermediates and final synthesized products were characterized by ^{1}H NMR, ^{13}C NMR, and HRMS (Fig. S30–S33†).

To verify whether the probe **HV-AS** can be used for synergistic fluorescence imaging of H_2O_2 and viscosity, the photophysical properties of **HV-AS** were first detected before and after reaction with H_2O_2 under physiological conditions. As shown in Fig. 1a, the characteristic absorption peak of **HV-AS** at 530 nm gradually rose after reaction with H_2O_2 (0–500 μM) accompanied by obvious color changes (Fig. S4†), and its molar extinction coefficient elevated from 180 to 6.79×10^3 L mol^{-1} cm^{-1}. Additionally, the fluorescence intensity of the probe at 680 nm also increased significantly (40.3-fold, $C_{H_2O_2} = 500$ μM), which shows a clear linear correlation with the concentration of H_2O_2 (0–80 μM, Fig. 1b). The linear equation is calculated as $F_{680} = 35.5 [H_2O_2](\mu M) + 214$ ($R^2 = 0.998$), and the detection limit toward H_2O_2 was 0.361 μM (Fig. 1c). The fluorescence quantum yield of **HV-AS** was 0.00100 and 0.201 before and after reacting with H_2O_2, respectively. These results indicate that **HV-AS** shows high sensitivity towards H_2O_2 and can be used for near-infrared detection of H_2O_2. Subsequently, the anti-interference ability and stability of **HV-AS** in response to H_2O_2 were further investigated. As shown in Fig. 1d and S5–S6,† after co-incubation of **HV-AS** with various bioactive molecules, the fluorescence change was negligible and showed specificity only to H_2O_2. When detecting H_2O_2 with **HV-AS** in the biologically relevant pH (6.5–8.5),[43] the activated fluorophore existed in a deprotonated form, which facilitated cyclization reactions. It

Scheme 1 The structure and sensing mechanism of **HV-AS**, and the signaling pathways involving H_2O_2 and viscosity. Created with https://www.biorender.com.

Fig. 1 *In vitro* optical properties of **HV-AS** (20 μM) in response to H_2O_2 and viscosity. (a) UV/vis absorption of **HV-AS** in the H_2O_2 channel. (b) Fluorescence spectra of **HV-AS** incubation with different concentrations of H_2O_2. (c) Linear correlation of **HV-AS** in response to H_2O_2 (0–80 μM). (d) Selectivity of **HV-AS** toward different analytes. The fluorescence intensity of the blank group was defined as 1. (e) UV/vis absorption of **HV-AS** in the viscosity channel. (f) Fluorescence spectra of **HV-AS** upon treatment with MeOH−glycerol systems (0.300−140 cp) (g) Linear correlation of **HV-AS** with different viscosities. (h) Selectivity of **HV-AS** toward different analytes in the viscosity channel. The fluorescence intensity of the blank group was defined as 1. H_2O_2 channel: $\lambda_{ex} = 570$ nm, $\lambda_{em} = 680$ nm, slit:10 nm, 10 nm. Viscosity channel: $\lambda_{ex} = 360$ nm, $\lambda_{em} = 537$ nm, slit: 5 nm, 5 nm.

enabled better detection of H_2O_2 under physiological conditions (Fig. S7†). The reaction kinetics of **HV-AS** exhibited good photostability after reactions with H_2O_2 (Fig. S8 and S9†). The above results all indicate that **HV-AS** has good specificity for the fluorescence detection of H_2O_2, which shows promise for imaging and detecting H_2O_2 in complex biological systems.

Next, the fluorescence response of **HV-AS** towards viscosity was investigated. As shown in Fig. 1e and S10,† in solution with high viscosity (methanol–glycerol system), a new absorption peak of **HV-AS** appeared at 426 nm (molar extinction coefficient $= 1.58 \times 10^4$ L mol^{-1} cm^{-1}) and the maximum emission was at 537 nm. The fluorescence intensity of **HV-AS** gradually increases along with increasing viscosity (Fig. 1f and Table S2†), and the fluorescence quantum yields of **HV-AS** in low-viscosity and high-viscosity media were 0.00250 and 0.0277, respectively. Moreover, the fluorescence intensity exhibited a good linear correlation with the medium viscosity (log η, 0.300–140 cp), which the linear regression equation is log $F_{537} = 0.513\log \eta + 2.37$ ($R^2 = 0.997$, Fig. 1g). These results indicate that **HV-AS** can sensitively respond to changes in viscosity. It's worth noting that, in high-viscosity media, the response of **HV-AS** to viscosity gradually decreased along with increasing H_2O_2, indicating a structural change, and at the same time proving that malononitrile is the group responsible for the viscosity response (Fig. S11†). The selectivity and photostability of **HV-AS** were studied further. In a medium with low viscosity, the fluorescence of **HV-AS** at 537 nm was always weak no matter what analytes were added into the medium (Fig. 1h and S12†), but once in a medium with high viscosity, the fluorescence of **HV-AS** was raised up and stable within 30 minutes (Fig. S13†). These experiments collectively confirm that **HV-AS** is a highly sensitive and specific tool for assessing changes in viscosity.

Cellular fluorescence imaging of H_2O_2 and viscosity

We first investigated the biocompatibility and hemocompatibility of probe **HV-AS**. The MTT results suggested that cell viability was unaffected even when incubating with high levels of **HV-AS** (80 μM) (Fig. S14†). *In vivo* testing of male C57BL/6J mice procured directly from Nanjing GemPharmatech LLC, aged 4 weeks and weighing between 15–20 g was performed. All animal procedures were performed in accordance with the Guidelines for Care and Use of Laboratory Animals of Shandong Normal University and approved by the Animal Ethics Committee of Shandong Normal University (AEECSDNU2024016). The body weight of mice showed no abnormal changes, and H&E staining revealed no significant tissue damage, confirming that **HV-AS** has great biocompatibility and hemocompatibility (Fig. S15†–S17). The photostability of the probe was also detected, and results indicated that **HV-AS** has good photostability in the mice macrophage cell line of RAW 264.7 cells (BNCC354753, purchased from BeNa Culture Collection, China), making it suitable for cellular applications (Fig. S18a–c†). To explore the subcellular distribution of the probe, we co-incubated cells with commercial organelle dyes and the probe. As shown in Fig. S19 and S20,† the red fluorescence of the probe (H_2O_2 channel) exhibited high

Pearson's colocalization coefficients with Mito-Tracker Green (Pr = 0.909), while the blue fluorescence of the probe (viscosity channel) did not exhibit obvious overlap with any organelle dye. Given that the probe lacks organelle-targeting groups, we suspect these results might be due to that H_2O_2 is enriched in mitochondria, as mitochondria is the major organelle of H_2O_2 production.[44,45]
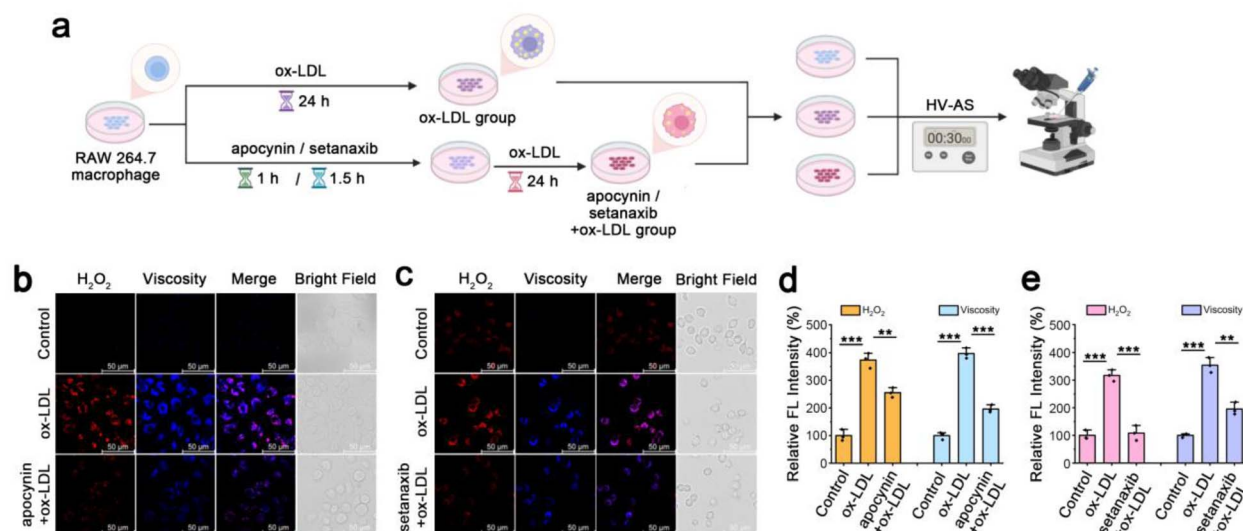
Next, to evaluate the probe's capability to image H_2O_2 and viscosity, we applied **HV-AS** in RAW 264.7 cells when under different stimulants. As shown in Fig. S21–S23,† stimulation with H_2O_2 enhanced the red fluorescence of the probe in cells 2.19-fold compared to the control group cells, while stimulation with Nystatin increased the blue fluorescence of the probe by approximately 3.02-fold. When cells were incubated with lipopolysaccharide (LPS), bright fluorescence was observed in both blue channels (3.16-fold for viscosity) and red channels (3.11-fold for H_2O_2), implying that LPS can induce oxidative stress and metabolic abnormalities in cells to rise H_2O_2 and viscosity levels.[46–49] All these results demonstrate that **HV-AS** is an excellent near-infrared dual-functional fluorescence probe, which can sensitively and selectively assess H_2O_2 levels and viscosity changes in cells.

Encouraged by the fluorescence performance of **HV-AS** in cells, the probe was further applied to explore the changes of H_2O_2 and viscosity levels during the process of foam cell formation. First, CD40 expression was examined by standard immunofluorescence staining (IF staining) methods to certify that RAW 264.7 macrophages were successfully transformed to foam cells after incubating with ox-LDL for 24 hours (Fig. S24a and b†).[50,51] Then, we performed fluorescence imaging of **HV-AS** at different time points of incubation of RAW 264.7 with ox-LDL (0, 8, 16, 24 hours). The fluorescence of **HV-AS** in both channels was gradually increased with prolonged incubation time, eventually reaching a 3.49-fold increase in the viscosity channel and a 3.36-fold in the H_2O_2 channel (Fig. S25a–c†).

Exploring the potential signaling pathway in foam cell formation

To explore a new signaling pathway related to oxidative stress for foam cell formation, we initially investigated the sources of H_2O_2 in foam cells. Previous research indicates that nicotinamide adenine dinucleotide phosphate oxidases (NADPH oxidases, NOXs) are the primary source of vascular superoxide anions ($O_2^{\cdot-}$), which can spontaneously convert to H_2O_2 or be catalyzed by superoxide dismutase.[52] Since apocynin was reported to be a selective inhibitor of NOXs in both phagocytic and non-phagocytic cells,[53,54] we inhibited the activity of NOXs using apocynin and investigated changes in H_2O_2 and viscosity through fluorescence imaging of **HV-AS** in foam cells (Fig. 2a). As depicted in Fig. 2b and c, both H_2O_2 and viscosity markedly decreased by 1.46-fold and 2.03-fold in apocynin pretreated foam cells compared to control foam cells, suggesting that NOXs were upstream regulators of H_2O_2 and viscosity. To further elucidate which NOX isoforms play a pivotal role, setanaxib, a NOX1/4 inhibitor, was employed to replicate the aforementioned experiments.[55] The results demonstrate that
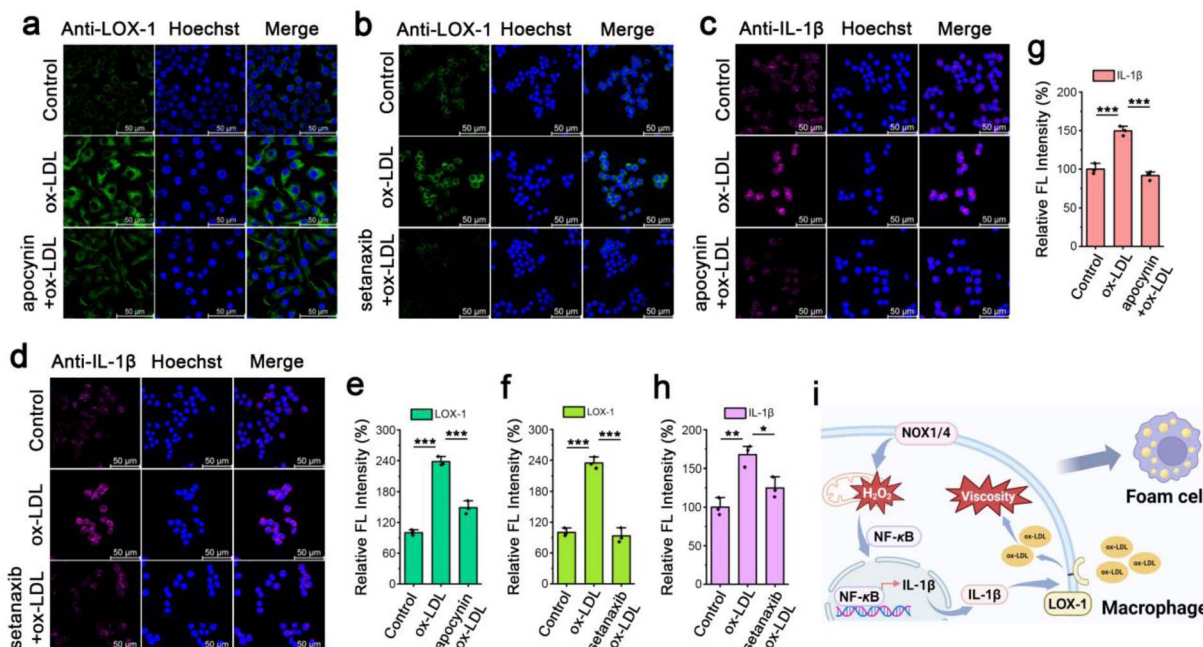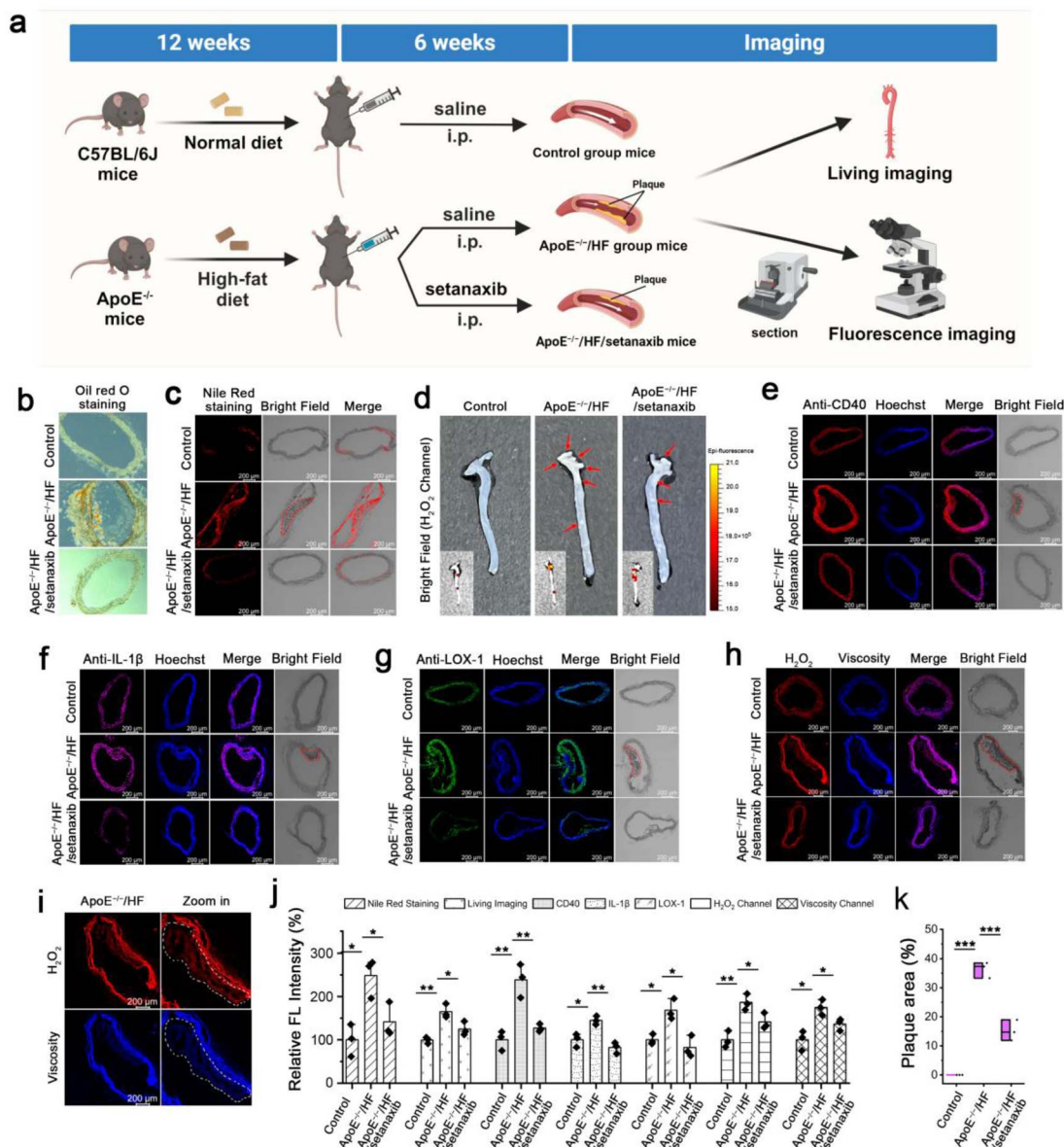
Fig. 2 Confocal fluorescence imaging of H_2O_2 and viscosity fluctuations in foam cells under different stimulations. (a) Construction of the cell model. Created with https://www.biorender.com. (b and c) Confocal fluorescence images of H_2O_2 (red channel: $\lambda_{ex} = 561$ nm, $\lambda_{em} = 570$–720 nm) and viscosity (blue channel: $\lambda_{ex} = 405$ nm, $\lambda_{em} = 420$–550 nm) in foam cells after incubation with apocynin (100 μM, 1 h) or setanaxib (10 μM, 1.5 h). (d and e) Relative fluorescence intensity (%) output of (b) and (c), respectively. The fluorescence intensity of the control group was defined as 100%. The data are expressed as the mean $\pm$ SD ($n = 3$). ***$p < 0.001$, **$p < 0.01$.

under setanaxib inhibition, not only foam cell formation delayed (Fig. 2d and e), but H_2O_2 and viscosity also decreased by 1.96-fold and 1.81-fold in cells, respectively. These findings strongly indicate that NOX1/4 likely serves as the primary source of H_2O_2, and also serves as an upstream positive regulator of H_2O_2 and viscosity in foam cells.

Fig. 3 Immunofluorescence imaging of LOX-1 and IL-1β. (a and b) Immunofluorescence images of LOX-1 and Hoechst 33342 indicated LOX-1 epitopes (green fluorescence) and nucleus (blue fluorescence) in the control group, ox-LDL group, apocynin + ox-LDL group cells or setanaxib + ox-LDL group cells, respectively. (c and d) Immunofluorescence images of IL-1β and Hoechst 33342 indicated IL-1β epitopes (purple fluorescence) and nucleus (blue fluorescence) in the control group, ox-LDL group, apocynin + ox-LDL group cells or setanaxib + ox-LDL group cells. (e–h) Relative fluorescence intensity (%) output of (a–d), respectively. (i) Signaling pathways involving H_2O_2 and viscosity. Created with https://www.biorender.com. Green fluorescence channel: $\lambda_{ex} = 561$ nm, $\lambda_{em} = 570$–720 nm; purple fluorescence channel: $\lambda_{ex} = 561$ nm, $\lambda_{em} = 570$–720 nm; blue fluorescence channel: $\lambda_{ex} = 405$ nm, $\lambda_{em} = 420$–550 nm. The fluorescence intensity of the control group was defined as 100%. The data are expressed as the mean $\pm$ SD ($n = 3$). ***$p < 0.001$, **$p < 0.01$, *$p < 0.05$.

Fig. 4 *In vivo* verification of signaling pathways. (a) Schematic diagram of mice model establishment. Created with https://www.biorender.com. (b) Oil red O staining of mouse vascular sections. (c) Nile Red staining of mouse vascular sections. (d) *Ex vivo* fluorescence imaging of **HV-AS** (H_2O_2 channel) in control group mice, $ApoE^{-/-}$/HF group mice and $ApoE^{-/-}$/HF/setanaxib group mice. (e) Immunofluorescence images of CD40 and Hoechst 33342 indicated CD40 epitopes (red fluorescence) and nucleus (blue fluorescence), respectively. Plaques are marked by red dotted curves. (f) Immunofluorescence images of IL-1β. (g) Immunofluorescence images of LOX-1. (h) Confocal fluorescence imaging of **HV-AS** in frozen sections from aorta. (i) Zoom in confocal fluorescent images of $ApoE^{-/-}$/HF group mice in (h), plaques are marked by white dotted curves. (j) Data output diagram of (b–h). (k) Data output diagram of plaque area (%) in (d). The fluorescence intensity of the control group was defined as 100%. The data are expressed as the mean ± SD ($n = 3$). ***$p < 0.001$, **$p < 0.01$, *$p < 0.05$.

The accumulation of cholesterol, which is a primary metabolite of ox-LDL, leads to increased viscosity, and the scavenger receptor LOX-1 serves as the primary receptor for ox-LDL entry into foam cells.[56] Therefore, we explored whether the activities of NOXs would influence expression levels of LOX-1 in foam cells. As shown in Fig. 3a, b, e and f, when foam cells were treated with apocynin or setanaxib, the immunofluorescence intensity of LOX-1 considerably lowered (1.60-fold or 2.51-fold), indicating that reduced NOX1/4 activity can severely down-regulate LOX-1 expression levels. Subsequently, we try to explore

the signaling pathway between NOXs and LOX-1. It is known that NOXs, the source of H_2O_2, can activate the NF-κB signaling pathway and increase pro-IL-1β expression, and therefore we first investigated whether the expression of IL-1β is influenced by NOX activity.[57–59] As expected, the immunofluorescence intensity of IL-1β also decreased (1.34-fold) in NOX-inhibitor pretreated cells (Fig. 3c, d, g and h). It is worth noting that IL-1β has been reported to regulate LOX-1 expression.[56] Based on these findings, it is evident that NOX1/4 plays a crucial role in foam cell formation (Fig. S26, S27a and b†). By generating

a substantial amount of H_2O_2 through NOX1/4, the NF-κB signaling pathway is activated, leading to increased IL-1β expression, which then activates LOX-1 expression, therefore promoting ox-LDL uptake and cholesterol accumulation, eventually viscosity increase and foam cell formation (Fig. 3i).

Validation of setanaxib effects *in vivo*

To verify this signaling pathway "NOX1/4–H_2O_2-NF-κB-IL-1β-ox-LDL uptake-viscosity" *in vivo*, we attempted to block the source of H_2O_2 to observe whether it could inhibit the formation of atherosclerotic plaques. Atherosclerosis was induced in mice by feeding ApoE$^{-/-}$ mice (purchased from GemPharmatech, China) a high-fat diet (ApoE$^{-/-}$/HF mice), while C57BL/6J mice were used as control group mice (C57BL/6J mice) (Fig. 4a). The NOX1/4 inhibitor setanaxib was used as an anti-atherosclerosis drug by reducing the generation of H_2O_2 to treat the atherosclerotic mice (ApoE$^{-/-}$/HF/setanaxib mice) (Fig. 4a). After 18 weeks, we compared the body weight and serum lipids (triglycerides TG, cholesterol CHO, high-density lipoprotein HDL, low-density lipoprotein–cholesterol LDL) among the three groups of mice, and performed oil red O and Nile red staining on vascular sections. Serum and vascular sections were isolated from C57BL/6J and ApoE$^{-/-}$ mice in the lab. As shown in Fig. 4b, c and S28,† serum lipid data of C57BL/6J mice were within normal limits, and its content on vascular sections suggested that this group mice did not suffer from atherosclerosis. As expected, the body weight and serum lipid data of ApoE$^{-/-}$/HF/setanaxib mice and ApoE$^{-/-}$/HF mice were elevated compared with those of C57BL/6J mice (Fig. S28 and S29†). However, it is noteworthy that the oil red O and Nile red staining results from ApoE$^{-/-}$/HF/setanaxib mice were similar to those of C57BL/6J mice, which were significantly lower (2.48-fold) than those of ApoE$^{-/-}$/HF mice (Fig. 4b and c). This result indicates that under setanaxib treatment, the severity of atherosclerosis in mice was prominently reduced compared to untreated mice, demonstrating a notable therapeutic effect of setanaxib. In order to more intuitively observe the extent of plaques by the naked eye in the blood vessels of mice, we dissected and fluorescence imaged the intact aortas of the mice. As indicated in Fig. 4d and j–k, the aortas of ApoE$^{-/-}$/HF/setanaxib mice were more transparent, had fewer plaques (2.49-fold), and exhibited weaker fluorescence (1.32-fold) compared to ApoE$^{-/-}$/HF mice, with all indicators approaching those of healthy mice. All the above results demonstrated that NOX1/4 inhibitor setanaxib could heavily postpone the generation of atherosclerotic plaque. Additionally, immunofluorescence staining of vascular sections for CD40, IL-1β, and LOX-1 also revealed that after inhibiting NOX1/4 expression with setanaxib, the expression of these proteins in ApoE$^{-/-}$/HF/setanaxib mice was suppressed (1.87-fold for CD40, 1.76-fold for IL-1β, and 2.04-fold for LOX-1) compared to those in ApoE$^{-/-}$/HF mice. Fluorescence imaging detection of vascular sections using **HV-AS** also showed a significant decrease in both H_2O_2 (1.31-fold) and viscosity (1.28-fold) (Fig. 4e–j). These data fully demonstrate that atherosclerotic mice treated with setanaxib exhibited excellent therapeutic effects due to the reduction in H_2O_2 levels, which hindered foam cell formation and prevented plaque development.

Conclusions

To elucidate the oxidative stress-caused lipid accumulation related signaling pathways involved in foam cell formation during early atherosclerosis, we exploited an ingenious near-infrared, dual-functional small-molecule fluorescent probe, **HV-AS**. This probe fluoresces in response to H_2O_2 (red fluorescence) and viscosity (blue fluorescence) with distinguishable spectra. By utilizing **HV-AS**, we revealed a novel signaling pathway of ox-LDL endocytosis in foam cells, which is the "NOX1/4-H_2O_2-NF-κB-IL-1β-ox-LDL uptake-viscosity" pathway, and validated these findings both in cells and *in vivo*. Based on this pathway, we also attempted to treat atherosclerotic mice using the NOX1/4 inhibitor setanaxib, and significant therapeutic effects were observed. We envision that **HV-AS** will benefit fundamental research into the pathogenic mechanisms of atherosclerosis, and provide a robust tool for evaluation of future atherosclerosis treatment and drug development.

Data availability

The data supporting this article have been included as part of the ESI.† All relevant data that support the findings of this study are available from the corresponding author upon reasonable request.

Author contributions

Hui Wang and Jingjing Guo contributed equally to this work. Hui Wang designed the probe, analyzed data and prepared the original draft. Jingjing Guo performed experiments, analyzed data and prepared the original draft. Tiancong Xiu performed parts of the experiments. Yue Tang, Ping Li and Bo Tang revised the manuscript. Wei Zhang and Wen Zhang analyzed data.

Conflicts of interest

There are no conflicts to declare.

Acknowledgements

Notes and references

1 L. G. Prado, N. O. S. Camara and A. S. Barbosa, *Front. Cell. Infect. Microbiol.*, 2023, **13**, 1148383.

2 D. Yin, Y. Zhong, H. Liu and J. Hu, *Int. J. Biol. Macromol.*, 2024, **270**, 132253.

3 N. Liu, C. Cui, Y. Sun, F. Zhang, S. Wang, G. Su and X. Cai, *Mol. Med. Rep.*, 2017, **16**, 6128–6133.

4 G. Schmitz and M. Grandl, *Antioxid. Redox Signaling*, 2007, **9**, 1499–1518.

5 K. J. Moore, S. Koplev, E. A. Fisher, I. Tabas, J. L. M. Björkegren, A. C. Doran and J. C. Kovacic, *J. Am. Coll. Cardiol.*, 2018, **72**, 2181–2197.

6 X. H. Yu, Y. C. Fu, D. W. Zhang, K. Yin and C. K. Tang, *Clin. Chim. Acta*, 2013, **424**, 245–252.

7 C. K. Lee, C. W. Liao, S. W. Meng, W. K. Wu, J. Y. Chiang and M. S. Wu, *Biomedicines*, 2021, **9**, 985.

8 J. F. Bentzon, F. Otsuka, R. Virmani and E. Falk, *Circ. Res.*, 2014, **114**, 1852–1866.

9 C. Van der Donckt, J. L. Van Herck, D. M. Schrijvers, G. Vanhoutte, M. Verhoye, I. Blockx, A. Van Der Linden, D. Bauters, H. R. Lijnen, J. C. Sluimer, L. Roth, C. E. Van Hove, P. Fransen, M. W. Knaapen, A. S. Hervent, G. W. De Keulenaer, H. Bult, W. Martinet, A. G. Herman and G. R. Y. De Meyer, *Eur. Heart J.*, 2015, **36**, 1049–1058.

10 S. E. Lee, H. J. Chang, J. M. Sung, H. B. Park, R. Heo, A. Rizvi, F. Y. Lin, A. Kumar, M. Hadamitzky, Y. J. Kim, E. Conte, D. Andreini, G. Pontone, M. J. Budoff, I. Gottlieb, B. K. Lee, E. J. Chun, F. Cademartiri, E. Maffei, H. Marques, J. A. Leipsic, S. Shin, J. H. Choi, K. Chinnaiyan, G. Raff, R. Virmani, H. Samady, P. H. Stone, D. S. Berman, J. Narula, L. J. Shaw, J. J. Bax and J. K. Min, *JACC Cardiovasc. Imaging*, 2018, **11**, 1475–1484.

11 K. Malekmohammad, E. E. Bezsonov and M. Rafieian-Kopaei, *Front. Cardiovasc. Med.*, 2021, **8**, 707529.

12 T. Liu, B. Xiao, F. Xiang, J. Tan, Z. Chen, X. Zhang, C. Wu, Z. Mao, G. Luo and X. Chen, *Nat. Commun.*, 2020, **11**, 2788.

13 E. Jose, W. March-Steinman, B. A. Wilson, L. Shanks, C. Parkinson, I. Alvarado-Cruz, J. B. Sweasy and A. L. Paek, *Nat. Commun.*, 2024, **15**, 3440.

14 M. C. Y. Chang, A. Pralle, E. Y. Isacoff and C. J. Chang, *J. Am. Chem. Soc.*, 2004, **126**, 15392–15393.

15 X. Liang, H. Li, X. Li, X. Tian, A. Zhang, Q. Luo, J. Duan, Y. Chen, L. Pang, C. Li, X. J. Liang, Y. Zeng and J. Yang, *Acta Pharm. Sin. B*, 2023, **13**, 372–389.

16 N. V. K. Pothineni, S. K. Karathanasis, Z. Ding, A. Arulandu, K. I. Varughese and J. L. Mehta, *J. Am. Coll. Cardiol.*, 2017, **69**, 2759–2768.

17 S. Singh and A. S. Gautam, *Curr. Atheroscler. Rep.*, 2019, **21**, 38.

18 A. Sharma, P. Verwilst, M. Li, D. Ma, N. Singh, J. Yoo, Y. Kim, Y. Yang, J. H. Zhu and H. Huang, *Chem. Rev.*, 2024, **124**, 2699–2804.

19 W. Zhang, F. Huo, F. Cheng and C. Yin, *J. Am. Chem. Soc.*, 2020, **142**, 6324–6331.

20 L. Teng, G. Song, Y. Liu, X. Han, Z. Li, Y. Wang, S. Huan, X. B. Zhang and W. Tan, *J. Am. Chem. Soc.*, 2019, **141**, 13572–13581.

21 Z. Huang, D. Wang, C. Y. Long, S. H. Li, X. Q. Wang and W. Tan, *J. Am. Chem. Soc.*, 2021, **143**, 8559–8564.

22 L. He, Y. Yang and W. Lin, *Anal. Chem.*, 2019, **91**, 15220–15228.

23 H. Li, W. Shi, X. Li, Y. Hu, Y. Fang and H. Ma, *J. Am. Chem. Soc.*, 2019, **141**, 18301–18307.

24 Y. Zhou, P. Li, X. Wang, C. Wu, N. Fan, X. Liu, L. Wu, W. Zhang, W. Zhang, Z. Liu and B. Tang, *Chem. Sci.*, 2020, **11**, 12149–12156.

25 W. Zhang, M. Li, X. Wang, W. Zhang, H. Wang, P. Li and B. Tang, *Anal. Chem.*, 2023, **95**, 2382–2389.

26 H. Wang, Z. He, Y. Yang, J. Zhang, W. Zhang, W. Zhang, P. Li and B. Tang, *Chem. Sci.*, 2019, **10**, 10876–10880.

27 M. Sang, Y. Huang, Z. Liu, G. Li, Y. Wang, Z. Yuan, C. Dai and J. Zheng, *ACS Sens.*, 2023, **8**, 893–903.

28 H. Wang, X. Zhang, P. Li, F. Huang, T. Xiu, H. Wang, W. Zhang, W. Zhang and B. Tang, *Angew. Chem., Int. Ed.*, 2024, **136**, e202315861.

29 M. Sang, Y. Huang, L. Wang, L. Chen, Nawsherwan, G. Li, Y. Wang, X. Yu, C. Dai and J. Zheng, *Adv. Sci.*, 2023, **10**, 2207066.

30 Y. Ma, J. Shang, L. Liu, M. Li, X. Xu, H. Cao, L. Xu, W. Sun, G. Song and X. B. Zhang, *J. Am. Chem. Soc.*, 2023, **145**, 17881–17891.

31 L. Zhou, Z. Wang, L. Wang, X. Zhang and Y. Xiao, *J. Am. Chem. Soc.*, 2023, **145**, 28296–28306.

32 F. Wei, Y. Ding, J. Ou, X. Chen, L. Li, Q. Zhou, Q. Chen, Q. Wang, Y. Feng and X. Meng, *Anal. Chem.*, 2023, **95**, 9173–9181.

33 J. Li, N. Zhao, W. Zhang, P. Li, X. Yin, W. Zhang, H. Wang and B. Tang, *Angew. Chem., Int. Ed.*, 2023, **135**, e202215178.

34 N. Wen, J. Li, W. Zhang, P. Li, X. Yin, W. Zhang, H. Wang and B. Tang, *Angew. Chem., Int. Ed.*, 2023, **62**, e202302161.

35 Y. Ma, W. Sun, Z. Ye, L. Liu, M. Li, J. Shang, X. Xu, H. Cao, L. Xu, Y. Liu, X. Kong, G. Song and X. Zhang, *Sci. Adv.*, 2023, **9**, eadh1037.

36 Y. Chai, L. Shangguan, H. Yu, Y. Sun, X. Huang, Y. Zhu, H. Y. Wang and Y. Liu, *Adv. Sci.*, 2024, **11**, 2304994.

37 Y. Zhou, P. Li, X. Wang, C. Wu, N. Fan, X. Liu, L. Wu, W. Zhang, W. Zhang and Z. Liu, *Chem. Sci.*, 2020, **11**, 12149–12156.

38 P. Ning, P. Dong, Q. Geng, L. Bai, Y. Ding, X. Tian, R. Shao, L. Li and X. Meng, *J. Mater. Chem. B*, 2017, **5**, 2743–2749.

39 R. Guo, J. Yin, Y. Ma, G. Li, Q. Wang and W. Lin, *Sens. Actuators, B*, 2018, **271**, 321–328.

40 Y. Zhou, Z. Liu, G. Qiao, B. Tang and P. Li, *Chin. Chem. Lett.*, 2021, **32**, 3641–3645.

41 P. Wang, Q. Gong, J. Hu, X. Li and X. Zhang, *J. Med. Chem.*, 2020, **64**, 298–325.

42 X. Liu, L. He, L. Yang, Y. Geng, L. Yang and X. Song, *Sens. Actuators, B*, 2018, **259**, 803–808.

43 D. Maity, A. Raj, P. K. Samanta, D. Karthigeyan, T. K. Kundu, S. K. Pati and T. Govindaraju, *RSC Adv.*, 2014, **4**, 11147–11151.

44 R. J. Mailloux, *Antioxidants*, 2020, **9**, 472.

45 F. Addabbo, M. Montagnani and M. S. Goligorsky, *Hypertension*, 2009, **53**, 885–892.

46 T. Liang, D. Zhang, W. Hu, C. Tian, L. Zeng, T. Wu, D. Lei, T. Qiang, X. Yang and X. Sun, *Talanta*, 2021, **235**, 122719.

47 J. Yin, M. Peng and W. Lin, *Anal. Chem.*, 2019, **91**, 8415–8421.

48 Y. Ma, Y. Zhao, R. Guo, L. Zhu and W. Lin, *J. Mater. Chem. B*, 2018, **6**, 6212–6216.

49 Z. Zhan, Q. Lei, Y. Dai, D. Wang, Q. Yu, Y. Lv and W. Li, *Anal. Chem.*, 2022, **94**, 12144–12151.

50 F. Mach, U. Schönbeck, G. K. Sukhova, E. Atkinson and P. Libby, *Nature*, 1998, **394**, 200–203.

51 F. Mach, U. Schönbeck and P. Libby, *Atherosclerosis*, 1998, **137**, S89–S95.

52 A. Konior, A. Schramm, M. Czesnikiewicz-Guzik and T. J. Guzik, *Antioxid. Redox Signaling*, 2014, **20**, 2794–2814.

53 A. L. Sylvester, D. X. Zhang, S. Ran and N. S. Zinkevich, *Biomolecules*, 2022, **12**, 823.

54 S. S. Barbieri, V. Cavalca, S. Eligini, M. Brambilla, A. Caiani, E. Tremoli and S. Colli, *Free Radic. Biol. Med.*, 2004, **37**, 156–165.

55 S. P. Gray, J. C. Jha, K. Kennedy, E. Van Bommel, P. Chew, C. Szyndralewiez, R. M. Touyz, H. H. H. W. Schmidt, M. E. Cooper and K. A. M. Jandeleit-Dahm, *Diabetologia*, 2017, **60**, 927–937.

56 O. Hofnagel, B. Luechtenborg, K. Stolle, S. Lorkowski, H. Eschert, G. Plenz and H. Robenek, *Arterioscler. Thromb. Vasc. Biol.*, 2004, **24**, 1789–1795.

57 A. Rasheed and K. J. Rayner, *Endocr. Rev.*, 2021, **42**, 407–435.

58 M. Canton, R. Sánchez-Rodríguez, I. Spera, F. C. Venegas, M. Favia, A. Viola and A. Castegna, *Front. Immunol.*, 2021, **12**, 734229.

59 W. C. Yen, Y. H. Wu, C. C. Wu, H. R. Lin, A. Stern, S. H. Chen, J. C. Shu and D. T. Y. Chiu, *Redox Biol.*, 2020, **28**, 101363.